

Optimization of Non-Pyrolyzed Lignin Electrodes for Sustainable Batteries

Ujwala Ail, Jakob Nilsson, Mattias Jansson, Irina A. Buyanova, Zhixing Wu, Emma Björk, Magnus Berggren, and Xavier Crispin*

Lignin, a byproduct from the pulp industry, is one of the redox active biopolymers being investigated as a component in the electrodes for sustainable energy storage applications. Due to its insulating nature, it needs to be combined with a conductor such as carbon or conducting polymer for efficient charge storage. Here, the lignin/carbon composite electrodes manufactured via mechanical milling (ball milling) are reported. The composite formation, correlation between performance and morphology is studied by comparison with manual mixing and jet milling. Superior charge storage capacity with $\approx 70\%$ of the total contribution from the Faradaic process involving the redox functionality of lignin is observed in a mechanically milled composite. In comparison, manual mix shows only $\approx 30\%$ from the lignin storage participation while the rest is due to the electric double layer at the carbon–electrolyte interface. The significant participation of lignin in the ball milled composite is attributed to the homogeneous, intimate mixing of the carbon and the lignin leading the electronic carrier transported in the carbon phase to reach most of the redox group of lignin. A maximum capacity of 49 mAh g^{-1} is obtained at charge/discharge rate of 0.25 A g^{-1} for the sample milled for 60 min.

1. Introduction

The monopoly of using fossil energy source is tiring down the world. Fossil energy sources are limited and release greenhouse gases; moreover, mundialization of the fossil energy network leads to geopolitical conflict. Today, there is a trend for nations to use their own renewable energy sources therefore being more independent and fighting against climate change. However, the process of mass implementing them has a bottleneck: energy storage. In that context, there is surge in research toward utilizing sustainable, environmentally friendly, bio-based materials for electrochemical energy storage systems in large-scale stationary applications. Lignin is one of the abundant biopolymers that is in our focus. Lignin is obtained in large amounts as a by-product from the industrial processing of biomass to extract cellulose pulp

and to produce cellulosic fuels.^[1,2] Lignin is the glue between cellulosic fibers in woods and plants (Figure 1a,b) and constitute about 15–25% of the vegetal. Importantly, lignin acquires chemical properties based on its extraction method. Kraft and sulfite pulping processes are the two effective methods used in industry for lignin isolation and respectively produce kraft lignin (KL) and lignosulfonate (LS)^[3] and have different properties. LSs have a higher degree of sulfonation compared to KL, due to the presence of more sulfur groups. The molecular weight (M_w) of LSs is generally similar or higher than that of KL. Also, the sulfonated groups in LSs make them anionically charged and water soluble.^[3,4]


A substantial amount of research have been performed on the pyrolysis of lignin to synthesize carbon materials (carbon black, hard carbon, graphitic carbon) used as electrode materials in supercapacitors and alkali-ion batteries.^[5] In this article, we are only considering lignin in its pristine and non-pyrolyzed form. The interest in this pristine aromatic branched biopolymer (Figure 1c) for energy storage is due to the presence of a large amount of aromatic alcohol groups (hydroxyphenyl H-group, guaiacyl G-group, syringyl S-group, see Figure 1d) coming from the monomer units of lignin called monolignols (coumaryl alcohol, coniferyl alcohol, sinapyl alcohol). Once demethylated, the ortho-aromatic diols give rise to reversible electroactive redox properties^[6] that we aim to exploit in battery applications.

U. Ail, M. Berggren, X. Crispin
Laboratory of Organic Electronics
Department of Science and Technology (ITN)
Linköping University
Norrköping SE-60174, Sweden
E-mail: xavier.crispin@liu.se

J. Nilsson
Ligna Energy AB
Box 787, Norrköping 601 74, Sweden

M. Jansson, I. A. Buyanova, Z. Wu, E. Björk
Department of Physics
Chemistry and Biology (IFM)
Linköping University
Linköping SE-58183, Sweden

M. Berggren, X. Crispin
Wallenberg Wood Science Center
Department of Science and Technology (ITN)
Linköping University
Norrköping SE-60174, Sweden

 The ORCID identification number(s) for the author(s) of this article can be found under <https://doi.org/10.1002/adsu.202200396>.

© 2022 The Authors. Advanced Sustainable Systems published by Wiley-VCH GmbH. This is an open access article under the terms of the Creative Commons Attribution-NonCommercial-NoDerivs License, which permits use and distribution in any medium, provided the original work is properly cited, the use is non-commercial and no modifications or adaptations are made.

DOI: 10.1002/adsu.202200396

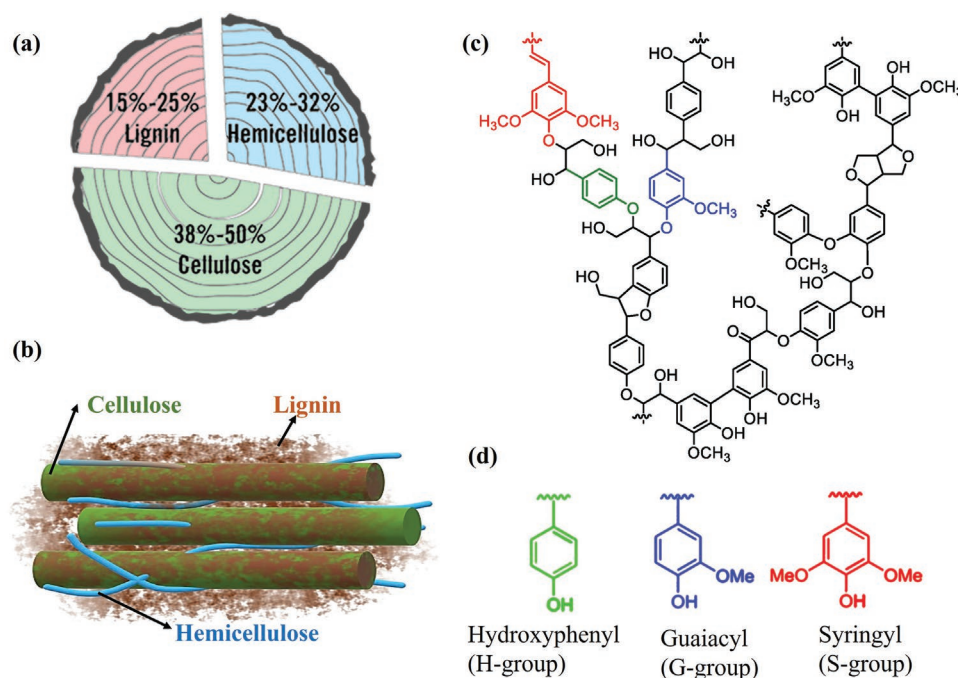


Figure 1. (a) and (b) are the schematic representation of lignin (red-lignin, green-cellulose, blue-hemicellulose), and (c) and (d) the chemical structure showing the monomeric units.^[7,8]

In aqueous acidic solutions, the catechol/quinone redox couple provides a reversible two-electron/two-proton reaction ($2e^-/2H^+$) (Figure 2a).^[4] Since lignin is an electrical insulator, it cannot transport electrons to proceed with the redox reaction. Hence, lignin needs to be combined with an electrical conductor such as conducting polymers,^[9–11] or different types of carbon structures such as graphene, partially reduced graphene oxide, carbon nanotube, partially reduced graphene oxide, graphite and conductive carbon.^[12–18] Figure 2 sketches a nanocomposite made of lignin and carbon nanosheets where electrons can be injected from the collector into the lignin electrode

and reach the catechol groups. To ensure charge balance, the cations (protons) are transported from the electrolyte into the swelled electrodes to reach the catechol redox site. This is the Faradaic contribution to the charge storage, which provides a peak in the cyclic voltammetry (CV) and a bump in the galvanostatic discharge (blue curve in Figure 2b). The Faradaic charge Q_F is carried by the lignin, while the capacitive contribution to the electric double layer charge Q_C is created at the carbon conductor/electrolyte interface. The latter is characterized by the square box (capacitive contribution) in the CV and the linear discharge in the galvanostatic curve (black

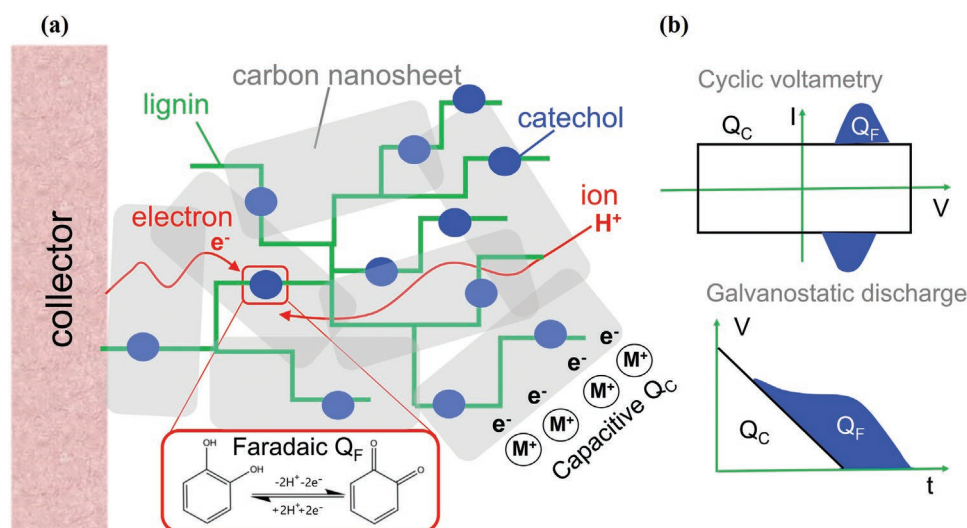


Figure 2. a) Pictorial representation of the nanocomposite made of lignin and carbon nanosheets with electronic and ionic pathways, and b) shows the effect of capacitive and Faradaic charge storage in CV and the galvanostatic discharge plots.

curve in Figure 2b). Chemical functional groups on lignin are key for the design of the composite. Positively doped conducting polymers will form an insoluble nanocomposite with the negatively charged LS during^[10] or after the synthesis of the conducting polymer.^[19,20] On the contrary, KL or desulfonated lignosulfonate (DSLS) made insoluble in water could be composed with carbon conductors. Che et al. found the Q_C/Q_F is of the range of 53/47 in their poly (3,4-ethylenedioxythiophene) (PEDOT)-LS composite.^[19] In our previous communication, we reported the composite of DSLS and carbon black via ball milling (mechanical milling) as an effective electrode material for aqueous energy storage systems. Ball milling was very effective in homogeneously mixing the components and bringing them in intimate contact at the nanometer scale. The comparison of the Faradaic and capacitive (non-Faradaic) contribution toward the total charge capacity was found to be 66% from the Faradaic contribution in case of ball milled DSLS and carbon black as compared to 11% in KL and carbon black.^[4,17] Mechanical milling has been reported in the literature as a route to make lignin carbon composites, wherein both KL and LS have been used.^[16,17] Ball milling is an effective and popular method used for the synthesis of equilibrium and non-equilibrium materials^[21] and even lead to some chemical reactions, for example, creating C–C bonds in organic solids due to high pressure and local heat generation.^[22] It has been employed to prepare and tailor carbon based materials to form tubular structure, closed-shell carbon nanoparticles, modify the carbon nanotube tip morphology,^[23–27] and exfoliate graphite into graphene.^[28] The effect of mechanical milling on the structure and amount of disorder on carbonaceous materials have been studied and been used for energy storage applications in Li-ion battery, supercapacitors, hydrogen storage, etc.^[29–32]

Here, we report on the role of the mixing method to create the lignin/carbon composite and investigate the interplay between morphology and the electrochemical property of the lignin electrode. Three methods of mixing are studied, namely manual mixing, jet milling and ball milling and their effect on charge storage capacity are discussed. In mechanochemistry various parameters affect the energy transferred to the molecular system (weight and type of balls, rotation speed, and

milling time); and the ideal morphology to bring electronic conduction to as many catechol units as possible is tuned also by the composition, that is, the ratio between the carbon and lignin. Finally, the porosity and the electric double layer formed at the carbon–electrolyte interface are the other key factors that decide about the ratio between the Faradaic and capacitive charge storage ability (Q_F/Q_C).

2. Results

2.1. Particle Size Distribution and Microstructural Analysis of the Composite

Figure 3a shows the particle size distribution of individual components and the composite powder of lignin and carbon black. Generally, carbon black has a characteristic particle morphology that consists of aciniform (grape-like) aggregates of highly fused spherical primary particles, with the aggregates clustered into larger-sized agglomerates with a size of more than 100 μm depending on the manufacturing methods.^[33,34] In the present case, carbon black powder (brown curve) shows binodal distribution in particle size with one contribution at 10 μm and one at 500 μm . The lignin powder (green curve) displayed a trinodal distribution with a small number of nanoparticles (≈ 300 nm), then two other overlapping contributions at 25 and 200 μm . When these two powders are manually mixed in a lignin-to-carbon black 1:1 weight ratio, the composite shows a particle size distribution (black curve) different than the carbon powder since the particles of 500 μm size were reduced into smaller ones. This indicates that the carbon particles in the 500 μm peak distribution were weakly bonded agglomerates made of the smaller ones (10 μm). The manually mixed composite has a trinodal distribution with a weak intensity peak likely coming from nanoparticles of lignin (≈ 300 nm), and two major contributions at ≈ 8 and ≈ 60 μm . Since the large particle size of lignin at 200 μm is absent, it is possible that this contribution was also a weak agglomerate of the small particles of 25 μm in the lignin only sample. Hence, one possible hypothesis could be that upon manually mixing the carbon powder with the lignin

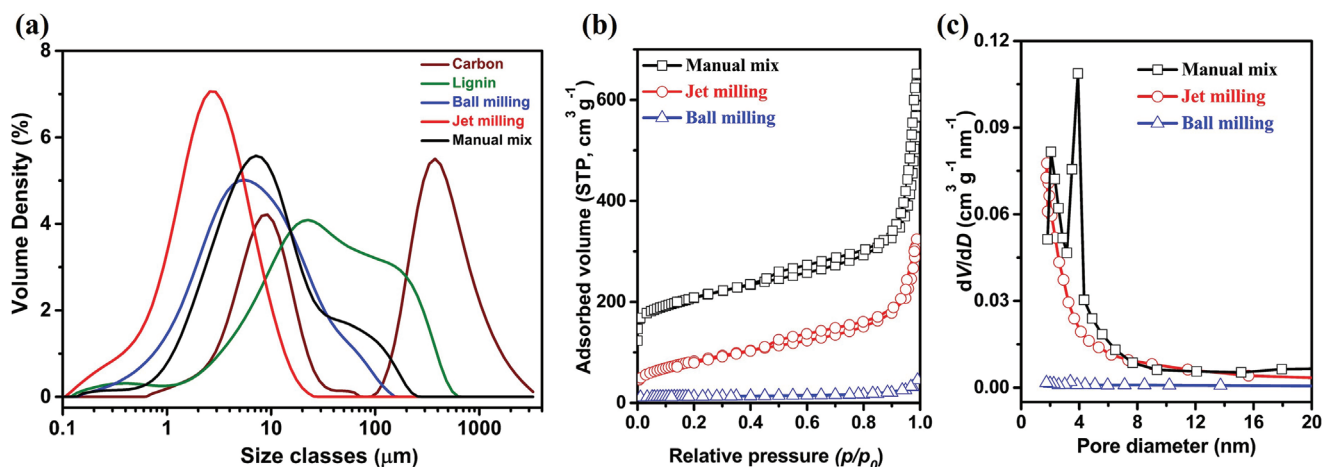


Figure 3. a) Particle size distribution in the pristine and the composite powder of lignin and carbon black, and (b) and (c) the physisorption isotherms and pore size distribution respectively.

powder, the hard carbon particles of 10 μm penetrate the soft large lignin of 25 μm to give new larger particles for the new contribution at 60 μm in the size distribution spectrum. Now, as soon as the power used for the mixing is larger, it is not reasonable to make any hypothesis, but we just make observations. The jet-milled samples (red curve), obtained from a lignin:carbon weight ratio equals to 1:1, show mostly one peak in the distribution with small average grain size $\approx 7 \mu\text{m}$. Note that there is a large increase in the density of sub-micrometer particle size compared to the ball milled (blue curve) and manually mixed (black curve) samples. The ball milled composite with the same 1:1 ratio shows particle size distribution in between the jet mill and the manually mixed distribution, with a broad peak centered at 5 μm and a shoulder at 50 μm . From this analysis, it is evident that jet milling produces finer composite particles than the other two mixing methods. In our previous study^[4] of the ball milled DSLS lignin/carbon composites, it was observed that, ball milled samples consist of grains that are coalesced with each other leading to a more compact, thus much less porous morphology compared to the manually mixed sample. Figures 3b and 3c show the physisorption isotherms and the pore size distribution of the composites. The nitrogen physisorption measurements of the powdered samples show drastic difference in the specific surface area between the ball milling and the other two milling methods. Ball milled samples show a specific surface of 11 $\text{m}^2 \text{g}^{-1}$, whereas the jet milled, and manually mixed samples show 300 and 390 $\text{m}^2 \text{g}^{-1}$, respectively. The source of the large surface area is not the lignin particles, (which are very compact), rather the carbon nano-powder (carbon black) which possesses an average specific surface area of about 780 $\text{m}^2 \text{g}^{-1}$ (supplier value). Hence the fact that the surface area of the manually mixed sample is still large, indicates that the lignin is not obstructing the nanopores

and that the carbon particles are not destroyed at the scale of the nanopores. However, when comparing the jet milling and ball milling methods, the ball milling is found to be more efficient in breaking apart the carbon particles and even removing the nano-porosity (Figure 3c) by mixing lignin and the broken carbon nanosheets in a very intimate fashion.

The surface morphology of the samples was studied using the scanning electron microscopy (SEM) with attached energy dispersive X-ray spectroscopic analysis (EDX) and is depicted in Figure 4a–c. In manually mixed samples (Figure 4a), the surface morphology is characterized by an apparent roughness due to tiny nano-grains of carbon black. These are the ones that provide the large surface density calculated by Brunauer–Emmett–Teller (BET) analysis. Interestingly, it is not possible to clearly distinguish the underlying lignin particles. Indeed, Figure 4d displays the EDX analysis of the manually mixed samples (black curve) with almost the same high carbon content on various points of the sample surface. This indicates the almost complete coverage of the lignin particles by carbon fine particles (also shown by corresponding low oxygen content). In contrast, in jet milled samples (Figure 4b) some of the lignin particles are exposed as visible by the light contrast of the image (related to the atomic density), which indicates a partial coverage of the lignin surface with carbon particles. This is supported by the significant variation in the carbon and oxygen contents on the surface from one point to the other (Figure 4d). We believe that in the manually mixed samples, the carbon particles are not destroyed but inserted into the soft lignin upon mechanical pressure. The jet milling mix provides tiny nanoparticles of lignin filling partially the nanoporosity of carbon, also large lignin particles are only partially covered by the carbon particles. The apparent nano-roughness of the jet milled sample is less than the manually mixed sample in agreement with the

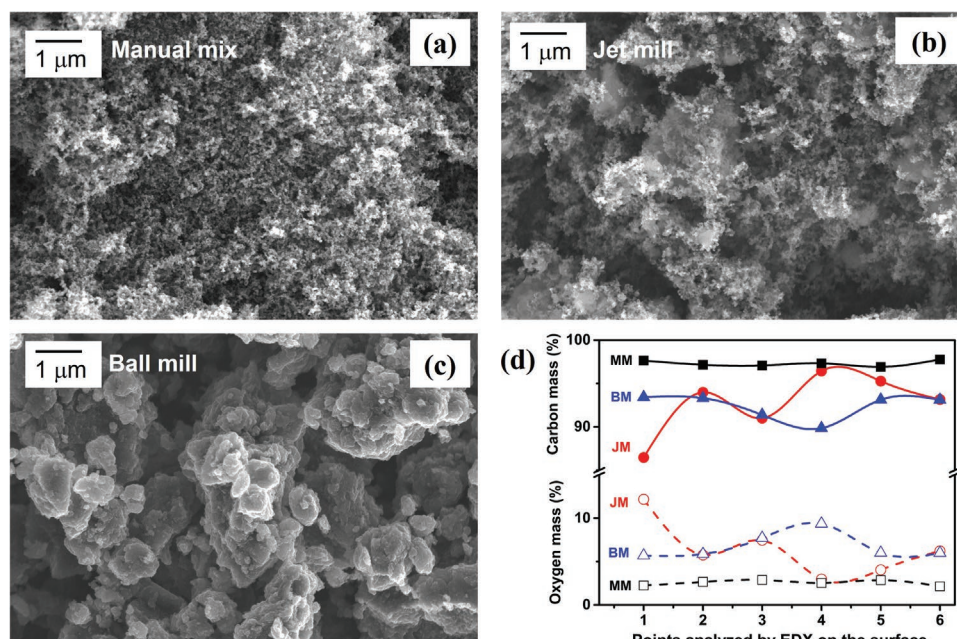


Figure 4. (a), (b) and (c) represent the surface morphology of the lignin/carbon composite powder mixed by manual mixing, jet milling and ball milling respectively and (d) is the point EDX on the random points on the sample surface (corresponding images of the EDX is given in Figure S1, Supporting Information). The sample names, JM, BM and MM correspond to the jet milled, ball milled and manually mixed composites respectively.

lower surface area density of the jet milled sample compared to the manually mixed sample. The third sample is the ball milled sample (Figure 4c) whose morphology is significantly different than the two others. There is a homogeneous mixing of the lignin and carbon so that the nano-roughness due to the presence of carbon nano-particles is not apparent anymore. This is because the particles have been broken in pieces and mixed with lignin. The compactness of the morphology is in agreement with the low surface area density. The same carbon-to-oxygen ratio is measured on several points on the surface of the ball milled sample, with a lower amount of carbon and a higher content of oxygen compared to the manually mixed sample. We conclude that ball milling provides an intimate mixing of broken pieces of carbon particles with lignin so that the morphology is compact and homogenous. The ball milled samples show better intermixing of the carbon and lignin compared to the jet milled and the manually mixed samples.

To identify if the mechanical energy provided during the mixing is enough to cleave the chemical bonds in the carbon particles and break them into pieces, we use Raman spectroscopy to analyze the vibrational signature of the carbon nano-objects. The powders are deposited on gold coated glass substrates. Normalized spectra of the first-order peaks from the three samples and the corresponding fitted spectra are shown in Figure 5a–c. Figure 5d displays the vibration mode of the carbon structure in the three samples. The sample prepared via ball milling clearly displays a shift in the two major peak positions and a change in peak intensity ratio. The fitting of those peaks was performed based on the studies by Mirosława et al.

and A. Sadezky et al.^[34,35] 2D materials like graphite possess a specific mode of vibration that can be analyzed to understand if the atomic environment of carbon atoms has been modified by the mixing. The G mode, corresponding to the mode of an ideal graphitic lattice, together with four defect modes, D1, D2, D3 and D4 are used and displayed in the figure. Peak positions were evaluated based on A. Sadezky et al.^[35] The G and D1 peaks were found to be slightly shifted in our data. Linear baseline correction was performed for all spectra prior to fitting. A Gaussian function was used to fit the D3 mode, while the other modes were fitted using Lorentzian functions.^[35] In the fitting procedure, the peak positions were kept constant when fitting all three spectra, while the peak intensities and widths were adjusted. The fit was performed to minimize the mean squared error. Compared to manually mixed and jet milled samples, a ball milled sample shows a shift in peaks toward a lower wavenumber and also show change in the intensity ratio (Figure 5d). The most pronounced difference is found in the ball milled sample compared to the two other samples. Indeed, the ball milled sample has a relative increase of the D3 peak, and a reduction of the G peak (Figure 5e). The D3 mode indicates the presence of amorphous carbon. The fitting therefore suggests that the carbon particles become more amorphous upon ball milling, thus supporting the existence of chemical cleavage as expected from breaking apart the carbon particles into small carbon nano pieces. The ratio $I_G/(I_{D1} + I_{D2} + I_{D3} + I_{D4})$ (Figure 5e) is proportional to the graphitic domain size, L_a . A slight decrease in this parameter is observed, showing that the graphitization does not increase, but possibly decreases

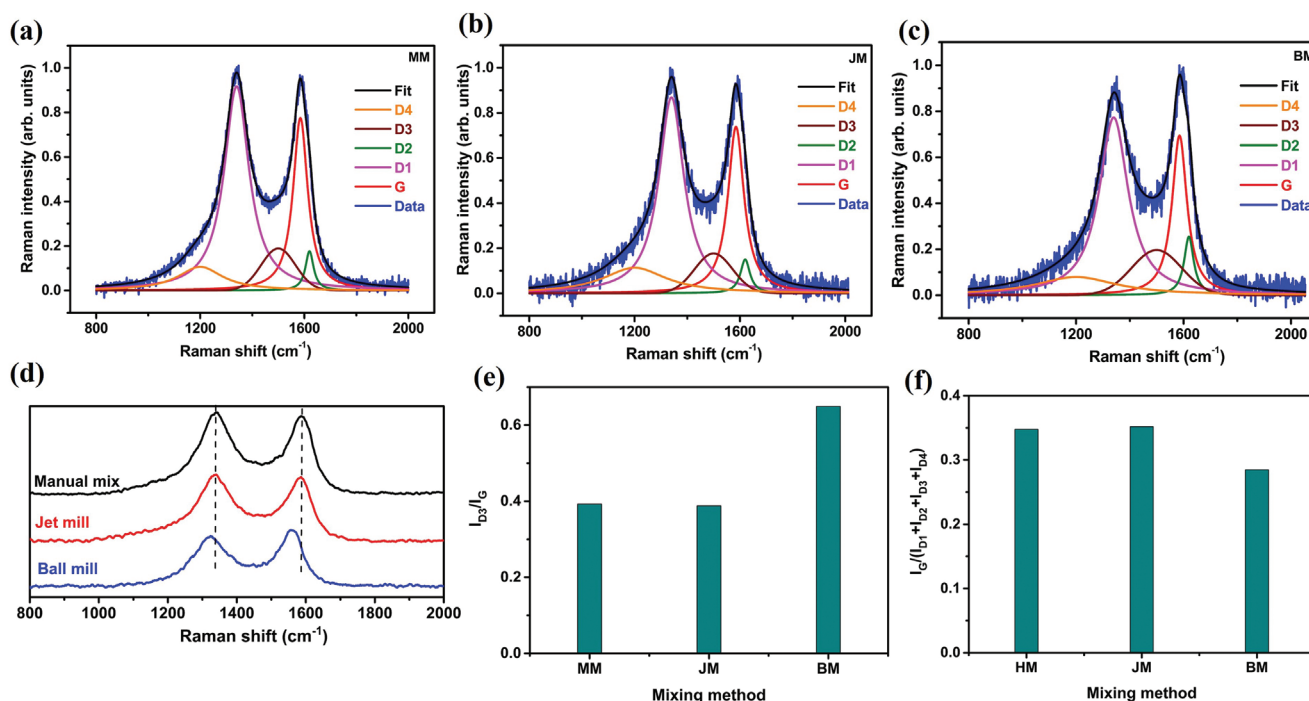


Figure 5. (a), (b) and (c) represent the normalized spectra of the first-order peaks from the manually mixed, jet milled and ball milled samples, respectively, d) compiled spectral comparison of the samples prepared by manual mixing, jet milling and ball milling, e) relative intensity of D3 and G peaks for the samples, and f) relative intensity of G band and other bands; $I_G/(I_{D1} + I_{D2} + I_{D3} + I_{D4})$ for different methods (full spectra shown in Figure S2, Supporting Information). The sample names, JM, BM and MM correspond to the jet milled, ball milled and manually mixed composites respectively.

with ball milling, which further supports the formation of tiny carbon nanosheets. We can find in the literature studies that further support this hypothesis. Indeed, ball milling has been used for preparing amorphous or nanocrystalline materials.^[21] The impact and the shear stress during the ball milling process results in the pulverization of the large bulk particles in addition to the amorphization of the crystal structure.^[36] For example, the changes in the crystallinity of graphite during milling has been studied on several occasions and the general conclusion was that graphite passes through a nanocrystalline phase prior to amorphization.^[23,37,38]

2.2. Effect of Mixing Methods on the Charge Storage Performance

Generally, there are two types of charge storage processes in these composites, one is due to the ions from the electrolyte being collected at the carbon surface forming an electric double layer giving rise to capacitive charge (non-Faradaic contribution); and the other in which electron transfer takes place at the interface between redox moiety (catechol) and the carbon (Faradaic contribution). As explained in the introduction (see Figure 1), both ions (protons from the electrolyte) and electrons are required for an efficient charge storage mechanism. To understand the effect of processing methods on the charge storage capacity of the composites, we first look at the CV of the electrodes in the aqueous 0.1 M HClO₄ electrolyte. CV data at a scan rate of 5 mV s⁻¹ are presented in Figure 6a for manually mixed (black curve), jet milled (red curve), and the ball milled

(blue curve) samples. The CV of the ball milled sample shows higher capacitive current (square-box, $I = -C \frac{dV}{dt}$) as well as higher Faradaic current than the jet milled and manually mixed samples. The large capacitive current indicates a large area at the carbon–electrolyte interface likely due to the breaking of the carbon in smaller pieces. The large Faradaic current suggests that electrons can be transported toward most of the catechol redox groups of lignin, which is possible because the lignin–carbon interface is maximized, and the electronic and ionic transport occur via percolation paths through the whole nanocomposite. The Faradaic and non-Faradaic contribution to the total charge storage are shown in the form of a bar chart in Figure 6b. The blue bars represent the exact capacity values with the patterned part showing the non-Faradaic capacity. Interestingly, even the non-Faradaic contribution of the ball milled sample (12.6 mAh g⁻¹) is larger than the manually mixed sample (8.5 mAh g⁻¹); which is a priori a bit unexpected since the manually milled sample possesses a larger BET surface area density (390 m² g⁻¹) compared to the ball milled sample (11 m² g⁻¹). This is a proof that the ball milled sample swells with the solvent and that ions penetrate the nanocomposite to form electric double layers around the broken pieces of the conducting carbon. Now the percentage ratio between the two mechanisms of charge storage (black bars) is also divided into the patterned region for the carbon (non-Faradaic) contribution and the empty bar for the lignin (Faradaic) contribution. The ball milled sample exhibits almost 70% of contribution from the Faradaic process and only 30% from the non-Faradaic, interfacial process. Ball milling promotes the spatial distribution

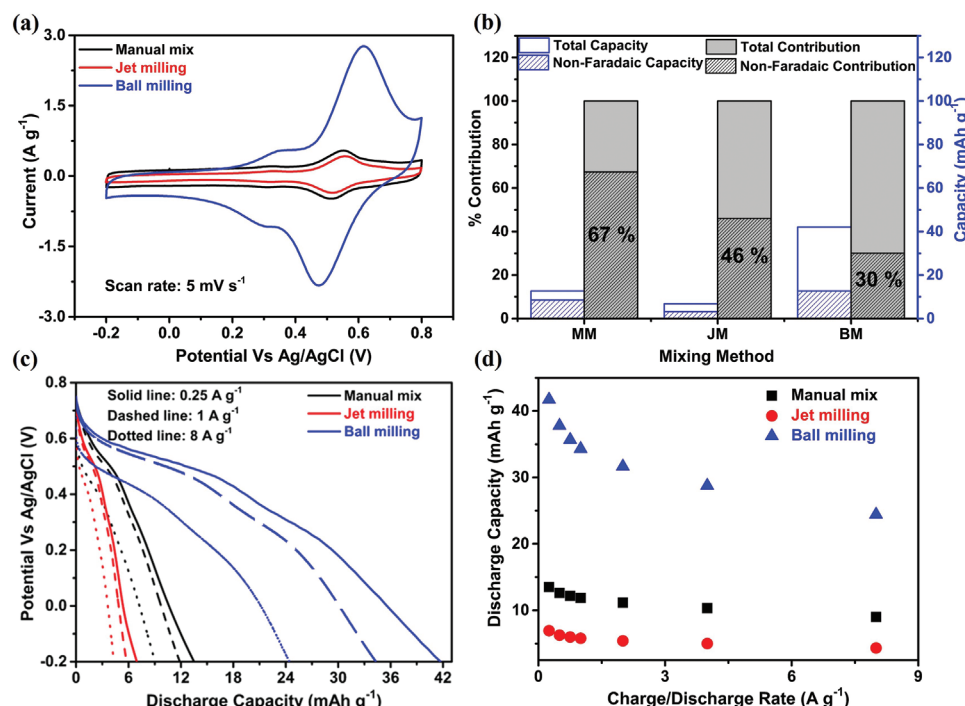


Figure 6. a) CV of the composite electrodes in 0.1 M HClO₄ at a scan rate of 5 mV s⁻¹, b) the capacity values (blue column) and the Faradaic and non-Faradaic contribution toward the total charge storage (black column). (c) is the galvanostatic discharge plots at charge discharge rates of 0.25, 1 and 8 A g⁻¹, and d) discharge capacity as a function of charge/discharge rates. The sample names MM, JM and BM indicate the composites prepared by manual mixing, jet milling and ball milling respectively.

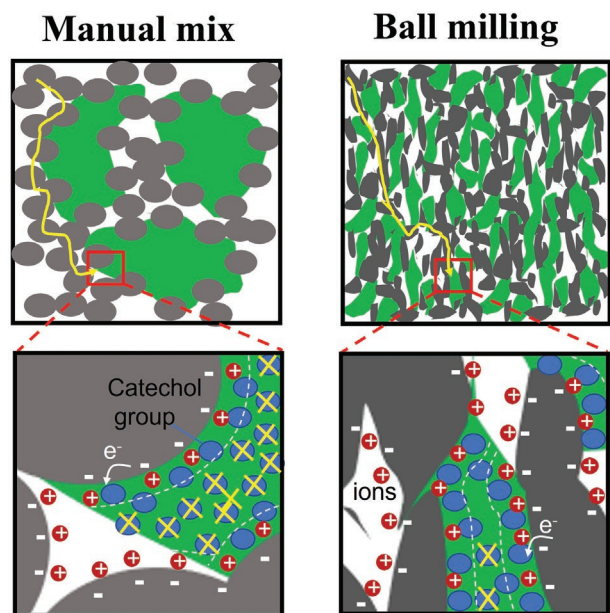


Figure 7. Schematic representation of the ball milling and manual mixing process and the corresponding charge storage mechanisms. The green phase is lignin, the gray phase is carbon, the blue circles are the redox groups in lignin and the red circles are the cations, the dashed lines represent the volume reachable by tunnel electron transfer from a carbon conductor surface into the lignin dielectric. The yellow crosses depict the non-electronically accessible redox groups of lignin.

of electronic transport paths through the swelled composite, thus enabling electron transfer from carbon to many redox active groups in lignin. On the other hand, the manually mixed sample shows 67% contribution from the non-Faradaic surface process toward the total charge storage capacity. In the sample prepared via manual mixing, the electric double layer is the dominant storage mechanism because the pristine nanoporosity of the carbon black remains in the composite and leads to a large carbon–electrolyte interface. Also, the carbon phase is not intermixed intimately with the electrically insulating lignin phase. As a result many redox groups in lignin cannot be accessed electrically and only the redox groups at the vicinity of the carbon phase are accessible for the Faradaic mechanism of charge storage. The morphology study indeed revealed that the carbon particles mostly cover the lignin particle surface, so lignin in the core of large particles is not reached by the electronic current. Figures 6c and 6d show the discharge plots and the discharge capacity as a function of charge/discharge rate, respectively, for different methods of mixing.

We picturize those storage mechanisms for the two extremes cases of ball milled and manual mixed samples in **Figure 7**. The measured Faradaic current will depend on the interface area between the carbon phase and the lignin phase. Indeed, only catechol groups in the lignin phase that are close to the carbon conductor connected to a percolation path can accept or lose electrons. Moreover, the distance between the carbon conductor and the catechol should be about a tunnel distance for electron transfer, so of the order of 1–2 nm.^[39–41] In those sketches, the green phase is lignin, the gray phase is carbon, the blue circles are the redox groups in lignin, the red circles are the cations

involved in the electric double layer at the negatively charged surface of the carbon particles. The dashed lines represent the volume reachable by tunnel electron transfer from a carbon conductor surface into the lignin dielectric. The yellow crosses depict the non-electronically accessible redox groups of lignin. In case of manually mixed samples, many catechol groups of lignin are not accessible by the electron transfer because they are too far from a carbon conducting percolation path.

Figure 6c shows the galvanostatic discharge plot for the composites at different charge/discharge rates, namely 0.25 (solid curve), 1 (dashed curve) and 8 A g^{−1} (dotted curve). The capacity is reduced by 41% for the ball milled sample when the rate is increased from 0.25 to 8 A g^{−1}, but jet milled and manually mixed samples show a better rate capability with only 33% reduction in manually mixed and 38% in jet milled samples. Figure 6d is the comparison plot of the discharge capacity as a function of charge/discharge rate. Note that all three samples respond without much drop in energy density even at high current density; which is a prerequisite for super-capacitor applications. Ball milled sample shows the largest specific energy of 21.7 Wh kg^{−1} at 0.25 A g^{−1} charge/discharge rate, while all other methods result in lower than 10 Wh kg^{−1} at the same rate.

2.3. Optimization of the Carbon and Lignin Ratio in Ball Milled Composite

As ball milling is the most efficient technique to produce an intimate mixing between the lignin phase and the carbon phase, it is legitimate to wonder about the optimal composition of the composite leading to the maximum specific capacity. The composition of the lignin/carbon nanocomposite is systematically varied by tuning the weight ratio of the mix of the two powders (lignin and carbon) deposited in the ball milling equipment. Ball milling was carried out by keeping all the other parameters identical (time, type of balls, rotation speed). After making electrodes of various compositions (20–80% of lignin) from the resulting ball-milled powder (see Experimental Section), CV and galvanostatic charge/discharge were carried out in 0.1 M HClO₄. When the lignin composition is 20%, the charge storage is dominated by capacitive nature of the conducting carbon forming electric double layers at the carbon–electrolyte interface (Figure 1). In the CV of **Figure 8a**, only small humps originating from the redox reaction of lignin are observed and the discharge curve is almost linear as expected from a capacitive character with a small shoulder at 0.5 V corresponding to the small Faradaic contribution of lignin (Figure 8b). Now, as the lignin amount increases in the composite, the features of lignin are enhanced: Faradaic peak in the CV and the plateau behavior in the discharge plot. Interestingly, by reporting the capacity versus the percentage of lignin, a parabolic behavior is found with a predicted maximum value of the capacity of 37 mAh g^{−1} at 45% (Figure 8c). Below that maximum, there is an excess in carbon particles that possess lower charge storage capacity (electric double layer) than lignin. Increasing the lignin content leads to an enhancement of the specific capacity by the Faradaic contribution of lignin. The optimum composition close to the 1:1 ratio corresponds to the

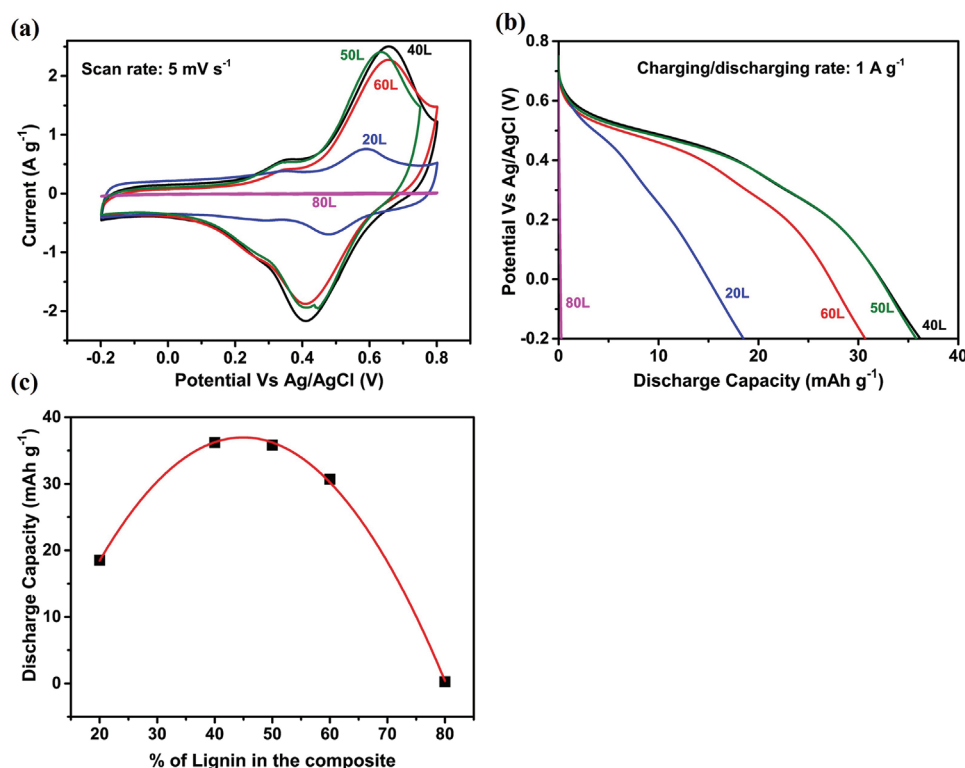


Figure 8. a) CV of the composite samples in 0.1 M HClO_4 at a scan rate of 5 mV s^{-1} , b) shows the galvanostatic discharge plot of the composites at a charge/discharge rate of 1 A g^{-1} , and c) the compilation of the performances as a function of lignin composition in the composite. Here all the composites are milled for 120 min. The polynomial fit is $y = ax^2 + bx + c$, $a = -0.0298$, $b = 2.6758$, $c = -23.1464$.

composition that maximizes the carbon–lignin interface area. At that composition the electronic transport through the carbon phase is good and many lignin redox sites are accessed. Above that optimum composition, the electrochemical performance of the composite decreases again due to the absence of enough carbon conductor to extract the stored charges, that is, the lignin starts to play the role of the insulator around some carbon

particles and cut the electronic percolation paths. The simplest argument for this optimum of specific capacity at 50% composition is provided by a simple model depicted in Figure 9a. 50% is the composition where the interface area between the lignin phase (blue) and the carbon phase (red) composite is maximum because this is at the interface that the catechol of lignin can be reached by the electron transfer from

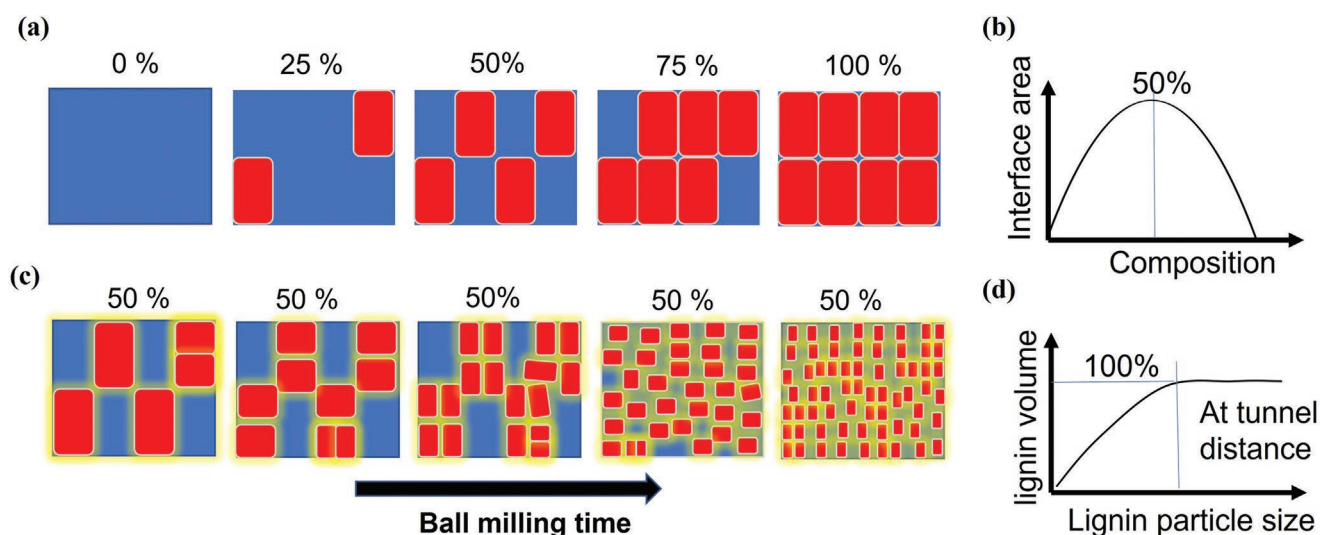


Figure 9. a) Sketch of the various lignin (blue)/carbon (red) ratio in the simple model composite with constant carbon particle size. b) Interface area versus composition. c) Sketch of the composite at 50% lignin/carbon ratio versus ball milling time. d) The volume of lignin accessible by the electron transfer versus the lignin particle size.

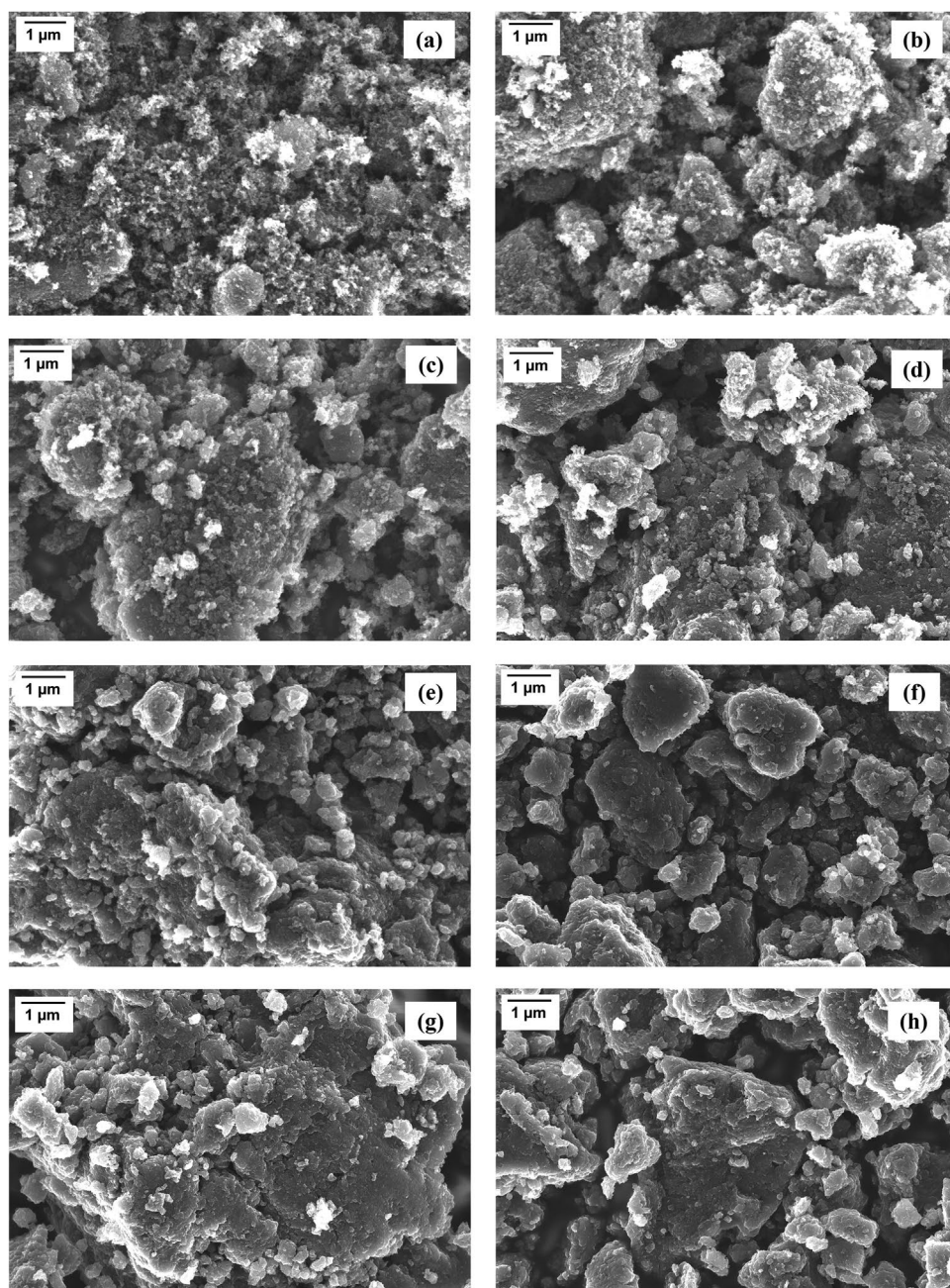


Figure 10. (a), (b), (c), (d), (e), (f), (g) and (h) show the SEM images of the composites milled for 5, 15, 30, 45, 60, 90, 105 and 120 min, respectively.

the carbon phase (lignin far away from the interface cannot be accessed). So, for a constant size of the carbon particles, the optimum capacity will always be for a composition of $\approx 50\%$ (Figure 9b). Now, for the same composition, it is possible to vary the interface area by tuning the size of the particles, which is the object of the next section.

2.4. Effect of the Ball Milling Time on the Electrochemical Behavior of the Composites

To further explore how the ball milling impacts the morphology and the charge storage performance, we mixed the

lignin–carbon in 1:1 weight ratio and follow the morphology and electrochemical performance versus the milling time while keeping the other milling parameters identical. **Figures 10a–h** show the SEM images of the composites milled for 5, 15, 30, 45, 60, 90, 105 and 120 min, respectively. The sample milled for 5 min (Figure 10a) shows two distinct surface features, one corresponding to the carbon nanoparticles appearing as a nano-roughness and the other to larger particles of lignin coated by carbon nanoparticles. As the duration of milling increases, the surface morphology changes gradually and after 60 min (Figure 10e) of milling, a homogeneous phase is observed. Even though the samples after 60 min of milling show wide distribution in the grain size, the

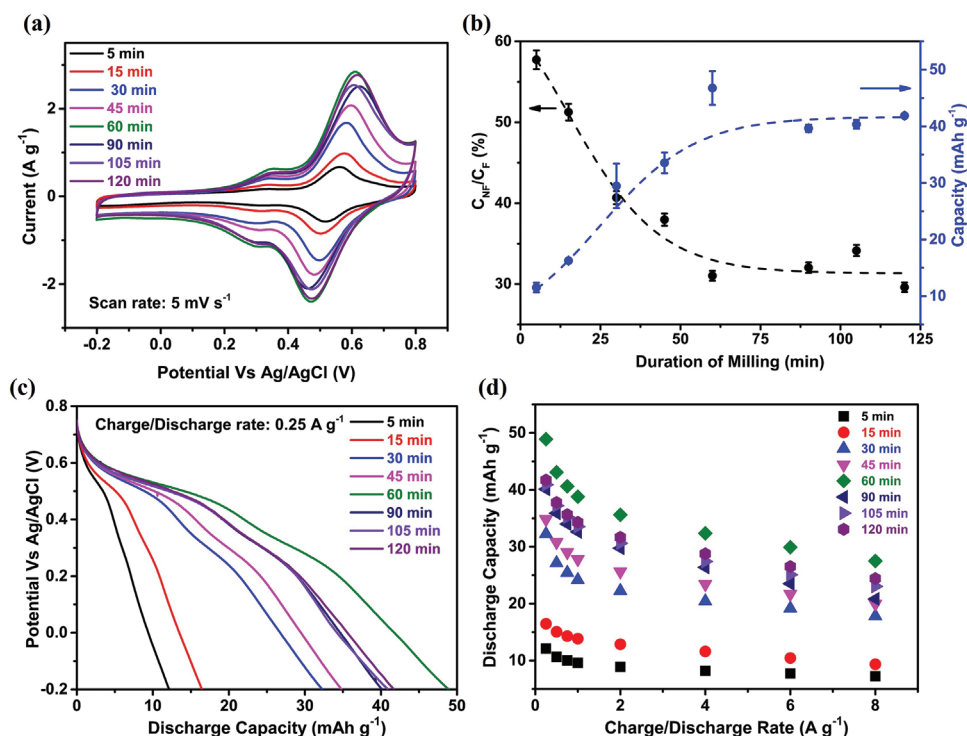


Figure 11. a) CV of the samples ball milled for different durations, b) ratio of Faradaic and non-Faradaic contribution as a function of milling time and the capacity as a function of milling time, (c) is the galvanostatic discharge plots at charge/discharge rates of 0.25 A g^{-1} , and d) discharge capacity as a function of charge/discharge rates.

carbon and the lignin phase cannot be distinguished. The EDX point analysis on the surface of 5 and 120 min milled samples is measured and presented in Figure S3, Supporting Information.

Figure 11a shows the CV of the composites milled for different durations. The Faradaic peak current rises with time and reaches a maximum at 60 min of milling; after that it slightly decreases and saturates. Corresponding charge contributions from the capacitive (non-Faradaic C_{NF}) and redox (Faradaic C_F) processes are compiled in Figure 11b. As seen for the ball milling time of 5 min, the total capacity is low (12 mAh g^{-1}) with a dominant contribution from the electric double layer at the carbon surface with $C_{NF}/C_F = 58\%$. For a longer milling time, the capacity shows sigmoidal behavior with a plateau at 42 mAh g^{-1} corresponding with a dominant Faradaic contribution with $C_{NF}/C_F = 30\%$. In between those two extremes, there is a transition from a capacitive to redox dominant character of the charge storage in the nanocomposite. In order to explain qualitatively the origin of the maximum plateau of the capacity versus ball milling time, we make a simple illustration of the composite in Figure 9c. The sketch represents a composite with a lignin:carbon ratio of 1:1. The ball milling breaks the carbon particle in smaller particles which increases the interface area between the carbon phase (red) and the lignin phase (blue). The total volume of lignin (blue) is constant because the composition 50% is constant. The electrons on the carbon can tunnel to a certain distance in the lignin which is illustrated by the yellow halo around the carbon particles. Hence the volume of lignin accessible by the electron tunnelling from the carbon phase is covered by the yellow halo and increases when the particle of carbon gets small. At a critical size, the interdistance

between the carbon particles becomes equal to the electron tunneling distance. Upon ball milling, the morphology changes to reach a threshold where the lignin phase located in between the carbon particle becomes fully accessible to the electron transfer (the blue area is fully covered by the yellow halo). Breaking the particles into an even smaller size does not change volume of lignin that is accessible since 100% is already reached. This explains in a simplified manner the maximum of the specific capacity versus ball milling time. Figure 11c shows the galvanostatic discharge plot at a charge/discharge rate of 0.25 A g^{-1} . As the duration increases, the capacity increases to 49 mAh g^{-1} at 60 min of ball milling after which the capacity decreases by $\approx 14\%$ for a higher milling duration of up to 120 min. This reduction might be due to the slight degradation of the sample due to the possible increase in temperature. Figure 11d shows the evolution of the discharge capacity as a function of charge/discharge rates for samples milled for different durations. Sample milled for 60 and 120 min show 44% and 42% reduction in capacity when the charge/discharge rate was increased from 0.25 to 8 A g^{-1} , indicating the degradation is not very pronounced. In terms of power and energy, the highest specific energy is 25 Wh kg^{-1} at 0.25 A g^{-1} and with a specific power of 3750 W kg^{-1} at 8 A g^{-1} for the 60 min ball milled sample.

Because CV is not a steady state method but a time-dependent method, the peak current and peak position in anodic and cathodic waves carry some information about the kinetics of the limiting mechanism. While these facts are well understood for simple systems like a mobile redox molecule diffusing in a liquid solution toward a planar metallic electrode

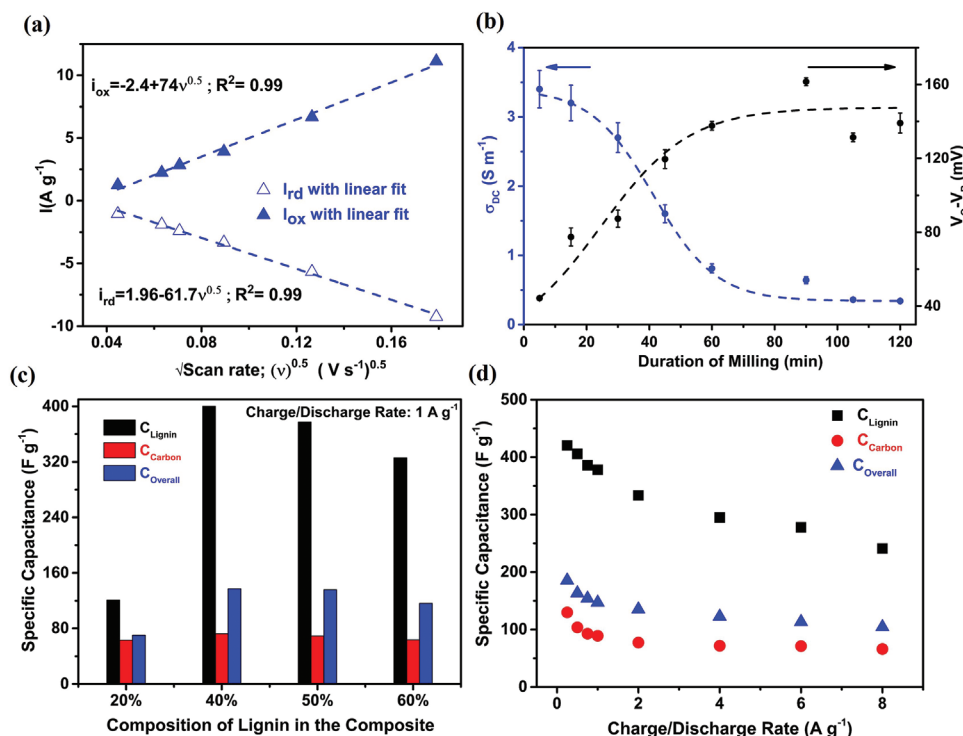


Figure 12. a) Peak current from CV (oxidation and reduction waves) versus square root of the scan rate. b) Electrical conductivity of the lignin–carbon composite and the peak-to-peak distance ($V_O - V_R$) as a function of milling time, c) decoupled values of specific capacitance of lignin and carbon determined from the discharge plot along with the overall value of capacitance for the composite with varying composition of lignin and carbon with a ball milling time of 120 min, and d) specific capacitance of lignin, carbon and overall value as a function of charge/discharge rate for the lignin/carbon composite of 1:1 composition milled for 60 min.

(Randles–Sevcik equation),^[42] our situation is different since the redox active molecule is an immobile catechol group attached to the insoluble lignin electrode. Since the catechol groups of lignin involve the transfer of two electrons and the transport of two protons at the same chemical group (proton-coupled electron transfer),^[43] the kinetics of the reaction depends on the slowest phenomenon involved. The latter can be: i) the electron transport in the percolation path of carbon, ii) the proton transport in the composite (possibly at the carbon–lignin interface) reaching the carbon surface and triggering the electron transfer, and iii) or the electron transfer itself. For the sample of highest capacity (ball milling time of 60 min), the Faradaic current intensity of both anodic and cathodic waves in the CV scales with the square root of the scan rate (Figure 12a). This is peculiar to the ball milled samples and it is not the case for other mixing methods (see Figure S4, Supporting Information). This feature indicates a diffusion limited mechanism. Since the redox groups are immobile, it is either the ionic transport or the electronic transport in the compact composite that limits the Faradaic current. In order to distinguish between those two mechanisms, we measured the DC conductivity of the electrode materials versus ball milling time. The DC conductivity is measured for a dry carbon–lignin layer with a 4-point probe method and it is dominated by the electronic transport as the non-solvated ions have typically very low conductivity. The electronic conductivity of the lignin–carbon composite (Figure 12b) is about 3 S m⁻¹ already after 5 min ball milling (which is much lower than the manually mixed composite 10 S m⁻¹). The electronic conductivity decreases according to a sigmoid

function to reach a plateau at ≈ 0.3 S m⁻¹. Now, the ionic conductivity of the electrolyte used in the CV characterization is about 1 S m⁻¹ for 0.1 M HClO₄.^[44] Hence, we see that the ionic conductivity is of the same order of magnitude than the electronic conductivity. The electronic conductivity is expected to decrease even further in a wet and swollen state, so that it is in principle possible that the electronic transport could be the limiting phenomenon. This is confirmed by plotting the DC conductivity of the dry composite versus the peak-to-peak distance ($V_O - V_R$) measured in the CV. This ($V_O - V_R$) is typically coupled to the kinetics of a phenomenon limiting the Faradaic current. A fast kinetics leads to a small ($V_O - V_R$). Interestingly, we observe an inverse one-to-one relationship between the DC conductivity and the ($V_O - V_R$) versus milling time (Figure S5, Supporting Information). This supports the hypothesis that electronic diffusion of carriers is limiting the Faradaic current in the CV.

Finally, we extract the specific capacitance of the individual phases: lignin (C_{Lignin}) and carbon (C_{Carbon}) with the values reported in the literature.^[9,13] Calculation of the specific capacitance is done according to a methodology published in the literature from the inverse of the slope of the discharge plot (see Figure S6, Supporting Information).^[9,13] The overall capacitance ($C_{Overall}$) is determined from the final discharge capacity at a given charge/discharge rate knowing the potential difference of operation.^[9] The comparison of C_{Lignin} and C_{Carbon} for composites of various lignin:carbon composition is found in Figure 12c (at a charge/discharge rate of 1 A g⁻¹ and 120 min milling time). As mentioned previously, the $C_{Overall}$ reaches a maximum between a 40–50% lignin composition. It

is important to note that the C_{Carbon} does not vary drastically when the composition is varied, however, C_{Lignin} increases with its percentage in the composite and reaches a maximum of 400 F g⁻¹ at 40%. Considering the weight fraction of lignin in the composite, we get a value of 1000 F g⁻¹ for pure lignin. This value is in close agreement with the reported value in the literature.^[9] Note that this theoretical value is exciting but devoid of true physical practical meaning since there is always a need of a conductor to extract charge from lignin. The $C_{\text{Lignin}}/C_{\text{Carbon}}$ ratio of 5.54 and 5.46 is obtained for 40% and 50% lignin composition respectively at 1 A g⁻¹. For a 60:40 lignin/carbon composition, $C_{\text{Lignin}}/C_{\text{Carbon}}$ of 5.16 is obtained (at 0.5 A g⁻¹) which is 1.55 times higher than the reported value of 3.32 for a composite of lignosulfonate/reduced graphene oxide^[13] of similar composition to 60:40 at the same as the charge/discharge rate. Figure S6, Supporting Information, also shows the compilation of the specific capacitance values for 1:1 lignin/carbon composite milled for different durations. It is important to note that the milling time shows significant influence on the C_{Lignin} contribution, showing an increase of up to 60 min after which the value is saturated. Figure 12d shows the decoupled specific capacitance contributions versus current density (for the 1:1 lignin/carbon composite milled for 60 min). The C_{Lignin} of 421 F g⁻¹ is obtained for 0.25 A g⁻¹ and 250 F g⁻¹ at 8 A g⁻¹.

3. Conclusion

In this study, we optimized the composition and morphology of the lignin–carbon electrode for battery applications; moreover the interplay of various mechanisms involved in the charge storage was revealed. The morphology was strongly dependent on the mixing methods namely; manual mixing, jet milling and ball milling. Microstructural and the elemental analysis on the sample surface show that ball milling is effective in forming the intimate contact between the carbon and lignin. 70% of the total capacity of the battery electrode comes from the redox process in lignin for morphology obtained by ball milling, in contrary for manual mixing, 70% of the capacity originates from the electric double layer at the carbon–electrolyte interface. Time evolution of the morphology and the effect of the composition were interpreted with simple intuitive models extracting the basic physical phenomena in action. A maximum capacity of 49 mAh g⁻¹ is obtained at charge/discharge rate of 0.25 A g⁻¹ for the sample milled for 60 min, with corresponding highest specific energy of 25 Wh kg⁻¹ and specific power of ≈3750 W kg⁻¹ at 8 A g⁻¹ (see Figure S7 and Table S1, Supporting Information). Further, the comparison of the specific capacitance contribution from lignin and carbon is done with the literature supporting the efficiency of the ball milling process to produce electronic percolation paths that have access to the lignin redox functionality through all the volume of the composite.

4. Experimental Section

Lignin and carbon black composites have been prepared by three methods, namely, manually mixing the components, ball milling and

jet milling. Weight ratios of the lignin and carbon were maintained as 1:1 for comparison of the three mixing methods. The carbon black used was ENSACO 360 G from IMERYS (BET surface area of 780 m² g⁻¹) and the kraft lignin (Lineo Prime) sample was procured from Stora Enso. Ball milling (mechanical milling) was carried out in a planetary mill, Retsch PM 100 using ZrO₂ milling media at 500 rpm speed for 120 min with ball/powder ratio of ≈10–20. Unless otherwise mentioned, the ball milled composite indicates the composite wherein the components were milled for 120 min. For the sake of comparison, the lignin/carbon composite electrodes were also prepared by manually mixing the lignin and carbon black powders in a 1:1 weight ratio using mortar and pestle. Jet milling was carried out at Glen Mills Inc., USA using Model 01 Jet Mill. Compressed air was used to propel the particles to collide and abrade against other particles. It was then captured using a one micron filter bag. It was run at 100 psi using normal compressed air at a feed rate of 60 g h⁻¹. All the mixing methods were carried at air ambient in dry conditions. After the components were mixed, the aqueous slurry was prepared using carboxymethyl cellulose-styrene-butadiene rubber (CMC-SBR) (6%) as binder system. For the detailed study of the evolution of the microstructure in ball milling method, the ratios and the time of milling was also varied. Microstructural studies were carried out using the dry powder. For the electrochemical characterization, the slurry was coated on to stainless steel current collectors which were pre-coated with a carbon coating, with a typical dry electrode loading of 2–3 mg cm⁻².

Raman measurements were performed using a 532 nm solid state laser as an excitation source (5.5 mW). A 50× (0.5 NA) objective lens was used to both focus the excitation light to a 1 μm diameter spot on the sample, and to collect the scattered light in a backscattering geometry. The scattered light was then filtered using a 532 nm edge filter, dispersed in a single grating monochromator, and detected using a Peltier cooled Si CCD camera (Horiba Synapse). The measurements were performed at room-temperature.

Particle size analysis was done using master sizer 3000 (Malvern Panalytical) using a dry powder dispersion unit and the microstructure of the powdered samples was studied by SEM (Zeiss Sigma 500 Gemini) along with the EDX spectroscopic analysis. The physiosorption measurement was carried out on a Micromeritics ASAP 2020 analyzer at –196 °C using N₂ as adsorbate. The powder sample was degassed at 110 °C for 5 h under vacuum prior to the analysis. The specific surface area was calculated by the BET method, and the pore size distributions were derived from the desorption isotherms using the Barret–Joyner–Halenda (BJH) method.

Electrochemical performance of the electrode was carried out using a computer controlled potentiostat (SP200, BioLogic). The electrodes were evaluated by the CV at different scan rates and the galvanostatic charge/discharge by applying different charging rates (mass normalized current) in a 3-electrode system under nitrogen atmosphere. The measurements were also carried out in ambient conditions. There were no significant changes in the electrochemical activity in both the atmospheres in the potential ranges used in the present study. A Pt mesh was used as counter electrode, potential was measured versus the Ag/AgCl reference electrode, and the electrolyte was 0.1 M HClO₄. The charge capacity (mAhg⁻¹) was obtained by dividing the product of the discharge time (in seconds) and the discharge current (in mA) by the product of 3600 and mass of the total electrode material (in grams). Specific energy (E) and specific power (P) were calculated using $E = \frac{1}{m} \int V dt$ and $P = \frac{E}{t}$,

respectively, where m is total mass, t is discharge time, i is discharge current and V is the potential. It is important to note that all the values are normalized by the total mass of the electrode.

Supporting Information

Supporting Information is available from the Wiley Online Library or from the author.

Acknowledgements

The authors thank the Knut and Alice Wallenberg Foundation (KAW 2019-0344, KAW 2020-0174) and the Wallenberg Wood Science Center. The authors' research environment thanks Vetenskapsrådet (2016-05990) and the Swedish Government Strategic Research Area in Materials Science on Functional Materials at Linköping University (Faculty Grant SFO-Mat-LiU No. 2009-00971). M.B. acknowledges the Wallenberg Scholar grants. The authors thank Peter Ringstad working at Ligna Energy AB for discussion, Stora Enso providing the kraft lignin samples, and Glen mill, USA, for the jet milling facility.

Conflict of Interest

The authors declare no conflict of interest.

Data Availability Statement

The data that support the findings of this study are available in the supplementary material of this article.

Keywords

ball milling, biopolymers, Faradaic and non-Faradaic charge storages, lignin-carbon composites, renewable energy storages

Received: September 15, 2022

Revised: October 30, 2022

Published online:

- [1] B. M. Upton, A. M. Kasko, *Chem. Rev.* **2016**, *116*, 2275.
- [2] J. L. Espinoza-Acosta, P. I. Torres-Chávez, J. L. Olmedo-Martínez, A. Vega-Rios, S. Flores-Gallardo, E. A. Zaragoza-Contreras, *J. Energy Chem.* **2018**, *27*, 1422.
- [3] T. Aro, P. Fatehi, *ChemSusChem* **2017**, *10*, 1861.
- [4] U. Ail, J. Phopase, J. Nilsson, Z. U. Khan, O. Inganäs, M. Berggren, X. Crispin, *ACS Sustainable Chem. Eng.* **2020**, *8*, 17933.
- [5] a) J. Zhu, C. Yan, X. Zhang, C. Yang, M. Jiang, X. Zhang, *Prog. Energy Combust. Sci.* **2020**, *76*, 100788. b) W.-J. Chen, C.-X. Zhao, B.-Q. Li, T.-Q. Yuan, Q. Zhang, *Green Chem.* **2022**, *24*, 565. c) J. Liu, H. Yuan, X. Tao, Y. Liang, S. J. Yang, J. Q. Huang, T. Q. Yuan, M. M. Titirici, Q. Zhang, *EcoMat* **2020**, *2*, e12019; d) J. Liu, H. Yuan, X.-B. Cheng, W.-J. Chen, M.-M. Titirici, J.-Q. Huang, T.-Q. Yuan, Q. Zhang, *Mater. Today Nano* **2019**, *8*, 100049.
- [6] M. Baloch, J. Labidi, *RSC Adv.* **2021**, *11*, 23644.
- [7] a) S. Wang, G. Dai, H. Yang, Z. Luo, *Prog. Energy Combust. Sci.* **2017**, *62*, 33; b) M. S. Karunaratna, R. C. Smith, *Sustainability* **2020**, *12*, 734; c) C. Serrano, J. A. Cecilia, C. García-Sancho, A. García, *Top. Curr. Chem.* **2019**, *377*, 26; d) R. Priyadarshinee, A. Kumar, T. Mandal, D. Dasguptamandal, *Environ. Sci. Pollut. Res.* **2016**, *23*, 23349.
- [8] S. Wang, Z. Luo, *Pyrolysis of Biomass*, De Gruyter, Berlin **2017**.
- [9] G. Milczarek, O. Inganäs, *Science* **2012**, *335*, 1468.
- [10] F. N. Ajjan, N. Casado, T. Rębiś, A. Elfving, N. Solin, D. Mecerreyes, O. Inganäs, *J. Mater. Chem. A* **2016**, *4*, 1838.
- [11] F. N. Ajjan, M. J. Jafari, T. Rębiś, T. Ederth, O. Inganäs, *J. Mater. Chem. A* **2015**, *3*, 12927.
- [12] X. Geng, Y. Zhang, L. Jiao, L. Yang, J. Hamel, N. Giummarella, G. Henriksson, L. Zhang, H. Zhu, *ACS Sustainable Chem. Eng.* **2017**, *5*, 3553.
- [13] S.-K. Kim, Y. K. Kim, H. Lee, S. B. Lee, H. S. Park, *ChemSusChem* **2014**, *7*, 1094.
- [14] G. Milczarek, M. Nowicki, *Mater. Res. Bull.* **2013**, *48*, 4032.
- [15] A. M. Navarro-Suárez, N. Casado, J. Carretero-González, D. Mecerreyes, T. Rojo, *J. Mater. Chem. A* **2017**, *5*, 7137.
- [16] L. Liu, N. Solin, O. Inganäs, *RSC Adv.* **2019**, *9*, 39758.
- [17] S. Chaleawert-umpon, T. Berthold, X. Wang, M. Antonietti, C. Liedel, *Adv. Mater. Interfaces* **2017**, *4*, 1700698.
- [18] S. Chaleawert-umponab, C. Liedel, *J. Mater. Chem. A* **2017**, *5*, 24344.
- [19] C. Che, M. Vagin, U. Ail, V. Gueskine, J. Phopase, R. Brooke, R. Gabrielsson, M. P. Jonsson, W. C. Mak, M. Berggren, X. Crispin, *Adv. Sustainable Syst.* **2019**, *3*, 1900039.
- [20] J. Edberg, O. Inganäs, I. Engquist, M. Berggren, *J. Mater. Chem. A* **2018**, *6*, 145.
- [21] Y. B. Li, B. Q. Wei, J. Liang, Q. Yu, D. H. Wu, *Carbon* **1999**, *37*, 493.
- [22] S. Mateti, M. Mathesh, Z. Liu, T. Tao, T. Ramireddy, A. M. Glushenkov, W. Yang, Y. I. Chen, *Chem. Commun.* **2021**, *57*, 1080.
- [23] J. L. Li, L. J. Wang, G. Z. Bai, W. Jiang, *Scr. Mater.* **2006**, *54*, 93.
- [24] F. Liu, X. Zhang, J. Cheng, J. Tu, F. Kong, W. Huang, C. Chen, *Carbon* **2003**, *41*, 2527.
- [25] X. H. Chen, H. S. Yang, G. T. Wu, M. Wang, F. M. Deng, X. B. Zhang, J. C. Peng, W. Z. Li, *J. Cryst. Growth* **2000**, *218*, 57.
- [26] Z. Kónya, J. Zhu, K. Niesz, D. Mehn, I. Kiricsi, *Carbon* **2004**, *42*, 2001.
- [27] Á. Kukovecz, T. Kanyó, Z. Kónya, I. Kiricsi, *Carbon* **2005**, *43*, 994.
- [28] W. F. Zhao, M. Fang, F. Wu, H. Wu, L. W. Wang, G. H. Chen, *J. Mater. Chem.* **2010**, *20*, 5817.
- [29] F. Salver-Disma, A. Du Pasquier, J.-M. Tarascon, J.-C. Lassegues, J.-N. Rouzaud, *J. Power Sources* **1999**, *81–82*, 291.
- [30] E. Gomibuchi, T. Ichikawa, K. Kimura, S. Isobe, K. Nabeta, H. Fujii, *Carbon* **2006**, *44*, 983.
- [31] H. Wang, T. Ikeda, K. Fukuda, M. Yoshio, *J. Power Sources* **1999**, *83*, 141.
- [32] T. Ichikawa, D. M. Chen, S. Isobe, E. Gomibuchi, H. Fujii, *Mater. Sci. Eng., B* **2004**, *108*, 138.
- [33] C. M. Long, M. A. Nascarella, P. A. Valberg, *Environ. Pollut.* **2013**, *181*, 271.
- [34] M. Pawlyta, J.-N. Rouzaud, S. Duber, *Carbon* **2015**, *84*, 479.
- [35] A. Sadezky, H. Muckenhuber, H. Grothe, R. Niessner, U. Pöschl, *Carbon* **2005**, *43*, 1731.
- [36] S. Zhang, Y. Cui, B. Wu, R. Song, H. Song, J. Zhou, X. Chen, J. Liu, L. Cao, *RSC Adv.* **2014**, *4*, 505.
- [37] J. Tang, W. Zhao, L. Li, A. U. Falster, W. B. Simmons Jr., W. L. Zhou, Y. Ikuhara, J. H. Zhang, *J. Magn. Reson.* **1996**, *11*, 733.
- [38] J. B. Aladekomo, R. H. Bragg, *Carbon* **1990**, *28*, 897.
- [39] W. S. Bao, S. A. Meguid, Z. H. Zhu, G. J. Weng, *J. Appl. Phys.* **2012**, *111*, 093726.
- [40] A. B. Oskouyi, U. Sundararaj, P. Mertiny, *Materials* **2014**, *7*, 2501.
- [41] C. Lia, E. T. Thostenson, T.-W. Chou, *Appl. Phys. Lett.* **2007**, *91*, 223114.
- [42] A. J. Bard, L. R. Faulkner, *Electrochemical Methods: Fundamentals and Applications*, 2nd ed., John Wiley & Sons, Hoboken, NJ **2001**.
- [43] C. Che, M. Vagin, K. Wijeratne, D. Zhao, M. Warczak, M. P. Jonsson, X. Crispin, *Adv. Sustainable Syst.* **2018**, *2*, 1800021.
- [44] J. Barr, R. J. Gillespie, E. A. Robinson, *Can. J. Chem.* **1961**, *39*, 1266.